Engineering Structures 253 (2022) 113809

Contents lists available at ScienceDirect

Engineering Structures

journal homepage: www.elsevier.com/locate/engstruct

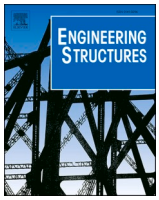

Response of a submerged floating tunnel subject to flow-induced vibration

P.X. Zou [a,b,c,*], Jeremy D. Bricker [a,d], L.Z. Chen [b,c], Wim S.J. Uijttewaal [a], Carlos Simao Ferreira [e]

[a] Dept. of Hydraulic Engineering, Faculty of Civil Engineering & Geosciences, Delft University of Technology, 2600GA Delft, the Netherlands
[b] CCCC FHDI Engineering Co., Ltd., Guangzhou, Guangdong 510230, China
[c] CCCC SFT Technical Joint Research Team, Zhuhai, Guangdong 519080, China
[d] Dept. of Civil and Environmental Engineering, University of Michigan, Ann Arbor, MI 48109, USA
[e] Department of Wind Energy, Delft University of Technology, 2600GA Delft, the Netherlands

ARTICLE INFO

Keywords:
Flow-induced vibration
Vortex-induced vibration
Submerged floating tunnel
Fluid structure interaction
CFD

ABSTRACT

In order to assess the dynamic performance of a submerged floating tunnel (SFT) subject to flow-induced vibration (FIV) conditions in a practical engineering application, a one-way fluid–structure interaction (FSI) model consisting of multi-scale hydrodynamic solvers combined with the finite element method (FEM) is established. A typical long, large aspect ratio SFT is modeled by coupling tube, joint, and mooring components. The SFT is simulated in the time domain under currents, waves, and extreme events. FIV of SFTs with different cross-section shapes is investigated by analyzing each structure's natural frequencies, hydraulic loading frequency, and dominant modes. The results show that FIV of the SFT tube is dominated by wave conditions. The excitation of the SFT's first dominant mode by a large wave height and period should be avoided. Standing and traveling wave patterns and multi-mode response are observed during extreme events. The hydrodynamic forcing and structural dynamic response of the SFT can be effectively reduced by adopting a parametric cross-section.

1. Introduction

The Submerged Floating Tunnel (SFT) is a novel long-distance sea-crossing infrastructure moored afloat from the seafloor and an alternative to immersed tunnels, bored tunnels, and bridges. The dynamic behavior of the SFT should be scrutinized to evaluate structural feasibility and reliability. The hydraulic loading on the SFT mainly includes currents, waves, and extreme events. Cross-flow (CF) and in-line (IL) flow-induced vibration (FIV) under different hydraulic loading cases become crucial factors, inducing structural fatigue damage and affecting the lifetime of the SFT. As water flows over the SFT tube and mooring lines, it causes an unsteady pressure field over the SFT surface and sheds an unsteady wake, which can excite FIV. If oscillatory flow due to vortex shedding periodically occurs and synchronizes with one of the structural natural frequencies, the SFT's amplitude of oscillation increases, leading to vortex-induced vibration (VIV), which is a category of FIV. VIV is associated with the so-called "lock-in" regime characterized by a shifting of vortex shedding frequency to the structural natural frequency. However, FIV research for the SFT remains in its infancy due to a series of key scientific challenges that have not been solved yet. The SFT is forced by a dynamic marine environment characterized by temporo-spatially varying hydraulic loading (e.g., typhoons), which brings challenges to the prediction of FIV for an SFT in engineering practice. Moreover, the SFT system is composed of a complex coupled mooring-tube-joint system [1]. Though a key component in SFT engineering design, the flexible joints between SFT segments have not yet been investigated in sufficient depth. In addition, potential SFT construction sites call for a tunnel length up to thousands of meters (e.g., 1.4 km at the Hogsfjorde crossing in Norway [2,3]; 3 km at Messina crossing in Italy [4]; 20 km at the Qiongzhou Strait in China [5]). A pragmatic approach to FIV research for such a long structure with a large aspect ratio (over 100) is still lacking.

In recent years, SFT-focused FIV research is appearing by means of experimental tests, theoretical and semi-empirical methods, and numerical simulations. For experimental investigations, since no SFT prototype has yet been built, only scale tests in laboratories have been carried out. Deng et al. [6] investigated cross-flow VIV features of a twin-tube SFT segment via a self-oscillating physical model test under steady flow. Yang et al. [7] experimentally analyzed the wave-current-induced motion response of a truncated SFT model. However, structural material and the Reynolds number of the flow are key factors affecting the FIV characteristics. The small laboratory scale limits generalizing the achieved results due to the inability to simultaneously guarantee all the similitudes involved. Thus, dynamic response of a

* Corresponding author.
E-mail address: p.zou@tudelft.nl (P.X. Zou).

https://doi.org/10.1016/j.engstruct.2021.113809
Received 19 March 2021; Received in revised form 14 December 2021; Accepted 26 December 2021
Available online 3 January 2022

prototype SFT cannot be simply determined by scaled-down experimental tests. For mooring lines or single cylindrical tubes, such as risers, pipelines, and sonar strings, which are characterized by intrinsic slender and flexible elements, abundant scientific studies exist [8–11]. However, experimental research considering the SFT tube and mooring lines as a coupled system subject to FIV are still scarce. As for theoretical and semi-empirical methods, Chen et al. [12] investigated the VIV response of a coupled SFT tube–cable system under hydrodynamic forcing based on the Hamilton Principle, in which the SFT tube and cables were simplified as supported Euler-Bernoulli beams without torsional behavior. Mai et al. [13,14] studied the effects of submergence depth, incident wave angle, and cross-section shape on the dynamic response of the SFT using potential flow theory and simplified the SFT as a spatial beam system. However, the physics of boundary layers, vortex shedding, and flow separation are not solved by using potential flow theory, and thus, the vortex-induced vibration conditions cannot be revealed. Hong and Ge [15] and Wu et al. [16] employed the wake oscillator model to determine the amplitude of vibration of the SFT tethers. VIVANA [17] and SHEAR7 [18] are also commonly used semi-empirical methods for VIV prediction in marine risers. However, these methods predict VIV based on empirical parameters obtained from large-scale experiments, while no abundant experimental results exist for the SFT. Moreover, with the addition of the mooring system and a buoyancy weight ratio (BWR) different from those of the experiments on which these methods are based, these semi-empirical tools for VIV prediction in risers and pipelines cannot be simply applied to the SFT. As for numerical methods, Chen et al. [19] explored mode competition and multi-mode VIV of the SFT using the finite element method (FEM), where the SFT was simplified as a flexible cylinder under a shear current. They used a third-order polynomial for the velocity of the structure to improve the Morison Equation. However, the coupled mooring and tunnel joint system was neglected. The FIV mechanism of the SFT is an intrinsic multi-physics issue with a strong interaction between the flow field and structure. A fully-coupled two-way fluid–structure interaction (FSI) simulation, in which data is exchanged between fluid and structural solvers at each time-step, can provide high-fidelity results for both structural response and flow field characteristics. However, the heavy computational burden of 2-way FSI makes it impractical for a prototype SFT simulation due to the great (multiple kilometers) tunnel length involved [20]. Therefore, in the context of practical design purposes, the one-way FSI technique is a pragmatic way to simulate FIV with the assumption that the flow field is not heavily affected by structural deformation. Abundant studies have demonstrated that one-way FSI is capable of providing plausible results for FIV predictions [21–24]. Therefore, in this study, the one-way FSI approach is applied for FIV prediction and analysis of the global dynamic response of an SFT.

In this paper, multi-scale hydrodynamic models considering the tempo-spatial randomness of the hydrodynamic loads along the SFT span are implemented. A model of a large aspect ratio, super-long SFT with coupled tube-joint-mooring components is established with two different cross-section shapes under a variety of hydrodynamic loads using FEM. This paper is structured as follows. Section 2 describes the methodology of combining multi-scale hydrodynamic models with an FEM solver for FIV prediction. Section 3 outlines the numerical validation and the model setup. Section 4 demonstrates the global dynamic response and prediction of FIV for the SFT forced by currents, waves, and extreme events.

2. Methodology

For a long span structure such as an SFT, the spatiotemporal variation and randomness of hydraulic loading (due to currents, waves, tides, extreme events, etc.) along the span must be considered in the engineering design. CFD, as the most comprehensive and accurate modeling approach, requires fine resolution and so is too computationally burdensome for simulation of stochastic waves varying along the span in a large domain. Therefore, a multi-scale cascade of models solving the large-scale oceanographic hydraulic conditions and the small-scale hydrodynamic forcing on the structure, is established. For large-scale oceanographic simulations, the integrated tide, ocean storm surge, and wave modeling framework of Delft3D-FLOW [25] coupled with SWAN is applied with a coarse grid size to obtain the hydraulic loading along the SFT span. However, detailed flow characteristics and structural forcing need to be computed with fine resolution at a small scale by CFD. Since CFD enables the pressure distribution over the SFT surface to be determined precisely, the numerically acquired water surface elevation and flow speed from Delft3D-FLOW simulations are imported as inlet-boundary conditions into the CFD model. With reference to the concept of strip theory (where the 3-D flow field along the structure is discretized into several two-dimensional fluid strips, or planes) applied to long flexible risers [26,27], the unsteady, spatially variable hydraulic loading can be specified at different locations along the span, improving the FIV prediction. As an effective numerical method in analyzing structure behavior, FEM is adopted for further analysis of the SFT dynamic response based on the hydrodynamic forcing calculated by the CFD. Using CFD in conjunction with FEM, motion of the structure, internal forcing, and FIV conditions can be assessed.

2.1. Hydrodynamic models

At a large scale, Delft3D-FLOW is a widely-used ocean-scale prediction tool for tsunami events, tidal flows, and storm surges, solving the depth-averaged shallow water equations based on the finite-volume method (FVM) [28,29]. At a small scale, most previous research [12,19,30,31] used the Morison equation for hydrodynamic modeling; however, this neglects the diffraction effect, which should be taken into account, especially for shorter waves. Furthermore, Morison equation coefficients are typically derived from experiments and restricted to simpler shapes. In addition, the Morison equation cannot provide flow field variables in detail. In this study, the CFD code ANSYS FLUENT v19.1 [32] is applied to conduct high-resolution two-dimensional field-scale simulations of the SFT by solving the unsteady Reynolds-averaged Navier-Stokes (URANS) equations using FVM. Due to the prototype scale of the SFT cross-section and the current speed in the deep sea, the Reynolds number is generally on the order of 10^7. This is suitable to the RNG k -ε turbulence model and wall layer used in the CFD simulations. The RNG k -ε model has been adopted for uniform current, regular wave, and extreme event modeling. Detailed governing equations of the RNG k -ε model, the volume-of-fluid (VOF) method, the applied Fifth-order Stokes wave theory, and the numerical computation domains, boundary settings, and model validations are described in [1,28] and [33].

2.2. Structural governing equations

The dynamic response equation for the SFT tube-joint-mooring system under hydraulic loading can be expressed as Eq.(1)

$$[M + M_a]\{..w^{\cdot}\} + [C]\{\dot{w}\} + [K_e + K_m + K_j]\{w\} = \{F\} \tag{1}$$

where $[\mathbf{M}]$ and $[\mathbf{M_a}]$ are the structural and added mass matrices, respectively; $[\mathbf{C}]$ is the damping coefficient matrix; $[\mathbf{K_e}]$, $[\mathbf{K_m}]$ and $[\mathbf{K_j}]$ are elastic stiffness of the SFT tube, mooring line, and joint stiffness matrices, respectively; $\{..\boldsymbol{w}^{\cdot}\}$, $\{.\boldsymbol{w}\}$ and $\{\boldsymbol{w}\}$ are the structural acceleration, velocity, and displacement vectors, respectively; $\mathbf{\{F\}}$ is the hydraulic loading vector.

For slender bodies such as SFTs, the three-dimensional added mass can be derived by integrating two dimensional added mass along the tube length [34]. The added mass is expressed as Eq. (2)

$$M_a = C_A \frac{\rho_w \pi D^2 L}{4} \tag{2}$$

where C_A is the added mass coefficient; ρ_w is water density; D is the

tunnel tube diameter; L is tube length.

The natural frequency is a key factor for structural dynamic response estimation. The vibration characteristics of the SFT, such as natural frequencies and corresponding vibration modes, can be obtained through modal analysis based on FEM using LUSAS v15.2 [35]. The presence of water around the tunnel tube creates an added mass due to the displacement of this water by the motion of the tube, and hence, the natural frequencies in water (wet natural frequencies) of the SFT system decrease compared with the natural frequencies in air (dry natural frequencies). The Eigen-frequencies and Eigen-mode equations of the SFT system in water can be calculated in the absence of external forcing, expressed as Eq. (3).

$$[K_e + K_m + K_j] - [M + M_a][\omega_{jj}^2] = 0 \tag{3}$$

where $[\omega_{jj}^2]$ is the diagonal matrix of the wet natural frequency of the SFT system.

For calculation of structural damping, Rayleigh damping is regarded as the most mathematically convenient model for structural dynamic response prediction, in particular for multi-degree-of-freedom systems [36]. The system of governing equations of motion in the case of linear response can be decoupled by the use of a modal transformation. Although the validity of Rayleigh damping assumption has not been thoroughly investigated, it is the most commonly used damping model in engineering practice [37]. Classical mass- and stiffness-proportional Rayleigh damping is formulated as Eqs.(4)-(6).

$$[C] = \beta_1[M + M_a] + \beta_2[K_e + K_m + K_j]. \tag{4}$$

$$\beta_1 = \xi\frac{2\omega_i\omega_j}{\omega_i + \omega_j}. \tag{5}$$

$$\beta_2 = \xi\frac{2}{\omega_i + \omega_j}. \tag{6}$$

where β_1 and β_2 are the Rayleigh damping coefficients; ξ is the modal damping ratio; ω_i and ω_j are the i^{th} and j^{th} mode wet natural frequencies of the SFT system, respectively.

3. Structural dynamic model

3.1. Model validation

3.1.1. Validation of natural frequency

To verify correctness and effectiveness of the natural frequency calculation for the SFT, the simulated results using modal analysis by LUSAS v15.2 [35] are compared with the case study from Jin et al. [31], which conducted a coupled tunnel-mooring line dynamic analysis using OrcaFlex [38]. The SFT length, diameter, and cross-sectional thickness are 900 m, 23 m, and 1 m, respectively. The mooring interval is 50 m. Both tunnel ends are fixed. The bending and axial stiffness of the tunnel tube are 1.26×10^{11} kN·m^2 and 2.07×10^9 kN, respectively. The added mass coefficient is 1.0. A schematic model of the SFT is shown in Fig. 1. Table 1 lists the validation results of the wet natural frequencies of the tunnel tube up to the 3rd mode. The maximum relative error is 3.45%, indicating the present numerical predictions of structural natural frequencies are reliable.

3.1.2. Validation of FIV prediction

To further verify the reliability of FIV predictions for the SFT using the current approach, the response amplitudes of a cylinder are compared with the results reported by Govardhan and Williamson [39]. A two-dimensional CFD model was established to obtain the hydrodynamic forcing on a fixed circular cylinder in a cross-flow, over the range of freestream velocities 0.04–0.40 m/s. The computational domain is 1.2 m in length and 0.4 m in height. A cylinder of diameter $D = 0.0381$ m is applied for the low mass-damping case. The first grid layer cell length

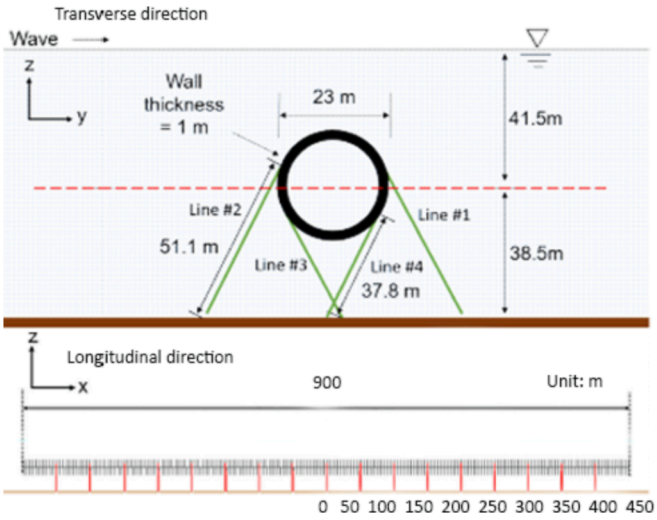

Fig. 1. 2D schematic views of the entire system for the validation case [31].

Table 1
Wet natural frequencies of the SFT validation case (Unit: rad/s).

Mode Number		ω_1 (Results from Jin et al.' s model [31])	ω_2 (Results predicted by LUSAS)	Relative error = $\frac{\lvert\omega_1 - \omega_2\rvert}{\omega_1}$(%)
Horizontal direction	1st mode	1.345	1.327	1.34
	2nd mode	1.630	1.598	1.96
	3rd mode	2.322	2.242	3.45
Vertical direction	1st mode	2.281	2.247	1.49
	2nd mode	2.455	2.412	1.75
	3rd mode	2.955	2.876	2.67

normal to the cylinder surface has a value of $y+$ close to 1 as required by the SST k-ω turbulence model (Fig. 2 (a)). The computational mesh is divided into 3 domains with different cell sizes. The first cell size (S_1): the cell size parallel to the SFT cross-section surface. The second cell size (S_2): the maximum unstructured mesh size around the SFT. The third cell size (S_3): the maximum structured mesh size in the rest of the domain. The grid independent limit test (GIL) is carried out by exemplifying the case freestream velocity of 0.40 m/s. The time histories of the calculated drag and lift using the three cell sizes are presented in Fig. 3, and the cell numbers and the calculated mean drag and the root mean square (RMS) lift force are listed in Table 2. It shows the lift force oscillation amplitude and frequency of all the three cases are consistent which are around 4.8 m and 2 Hz, respectively. However, the drag force of Case 1 is under-predicted compared with other two cases. Case 2 has almost identical results as Case 3 (thus is regarded as converged), while with fewer cell numbers and saves computational time. Therefore, grid settings of Case 2 are used for all case simulations. The vortex shedding frequencies for the static cylinder at different freestream velocities are over the range of 0.2–2 Hz and cover the system natural frequency. The calculated drag and lift are then transferred to the three-dimensional FEM solver LUSAS v15.2 for the FIV predictions.

In the structural dynamic model, the cylinder length L is 0.381 m with a length-diameter ratio of 10 (Fig. 2(b)). The mass ratio (the reciprocal of BWR) is 1.19, which is consistent with the experimental conditions [39]. The cylinder is modelled by "thick beam (BMS3)" elements with an element size of 0.01905 m. In the experiments, end plates were fixed to the test section and placed 2 mm below the bottom of the

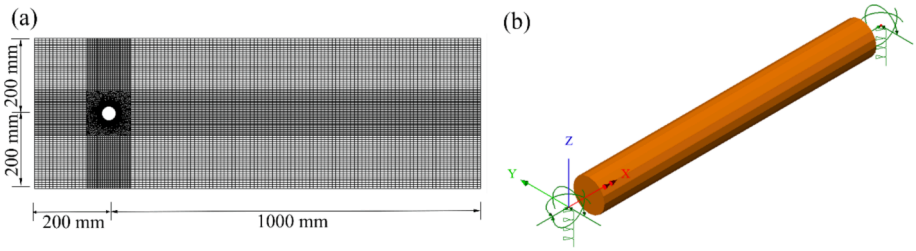

Fig. 2. Validation models. (a) Schematic Mesh of the CFD model; (b) Structural model using LUSAS v15.2 (a pair of vertical springs act on both ends).

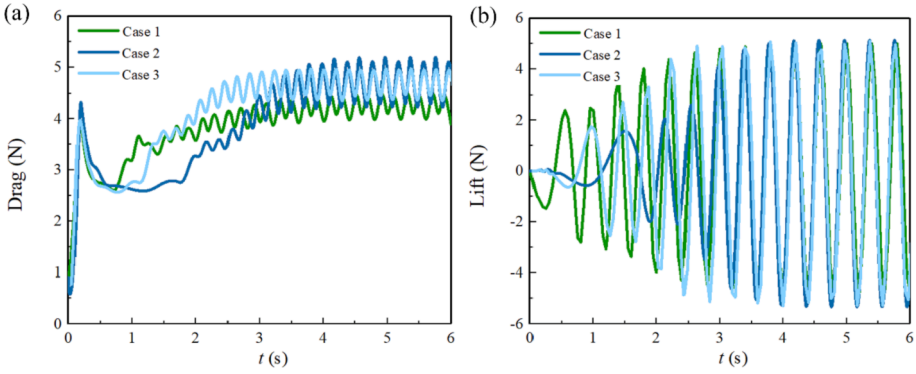

Fig. 3. The time histories of the calculated drag and lift for grid independent limit tests.

Table 2
Mesh size for the grid independent limit test.

	S_1 (mm)	S_2 (mm)	S_3 (mm)	N_{Cells}	*Mean Drag (N)*	*RMS Lift (N)*
Case 1	1	5	5	21,795	4.27	4.87
Case 2	1	2.5	5	28,103	4.62	5.08
Case 3	0.5	2.5	5	30,368	4.68	5.12

cylinder to encourage two-dimensional shedding, while in the numerical model, vertical springs with stiffness of 1270 N/m are set on both ends of the cylinder to provide the restoring forces [6]. The calculated drag and lift are uniformly distributed along the span and perpendicular to the longitudinal direction of the cylinder. Structural modal analysis is firstly performed to determine vibration characteristics (natural frequency, Rayleigh damping coefficients). The natural frequency of the cylinder in still water is 1.01 Hz. The structural damping ratio in water is 0.045, and as per Eqs. (4)–(6), β_1 and β_2 are 0.286 s^{-1} and 0.007 s, respectively. The detailed model parameters are listed in Table 3.

The onset of VIV can be assessed by a key non-dimensional parameter: reduced velocity V_R, expressed in Eq.(7)

Table 3
Model parameters for validation.

Parameter	Value
Cylinder diameter (m)	0.0381
Cylinder length (m)	0.381
Young's modulus (kPa)	45
Poisson's ratio (-)	0.167
Dry density (kg/m^3)	1190
Water density (kg/m^3)	1000
Added mass coefficient (-)	1.0
Structural damping ratio in water (-)	0.045
Spring stiffness for cylinder in CF direction (N/m)	1270
Natural frequency in still water (Hz)	1.01

$$V_R = \frac{V}{f_n D} \tag{7}$$

where V refers to the freestream velocity; f_n is the natural frequency of the structure in water.

Fig. 4 presents the simulated amplitude and frequency ratio of the numerical model compared with Govardhan and Williamson's results [39]. It shows that the simulated results are inconsistent with the experiments at both initial and upper branches. The amplitude ratio (defined by A/D, where A is the peak value of the oscillation amplitude of the cylinder) exhibits a jump during the transition between initial and upper branches at $V_R = 5$ (where the vortex shedding frequency is close to f_n). It proves that the vibration frequency ratio (defined by f/f_n, where f is the cylinder oscillating frequency during induced vibration) during synchronization lies above 1 [39]. Due to the assumptions of uniformly distributed hydraulic loading along the span and neglecting the actual surface roughness of the cylinder, dynamic response simulation of the SFT tube produces conservative results.

3.2. Model setup

3.2.1. Parameters of SFT cross-section

Steel shell-concrete (SSC) composite structures have been applied in advanced engineering constructions such as Kobe Port Minatojima [40] and ShenZhong Link [41], which have the merits of improving material properties, saving costs and manpower, and reducing the installation period and risk of seeping [40]. Hereby, similar technology can be used for the SFT. It is designed as a "sandwich structure" consisting of the outer and inner steel shells and filled concrete layer inside in the walls of the cross-section (Fig. 5). Longitudinal diaphragms and transverse webs can be implemented between the outer and inner steel plates. To simplify the input SSC material properties in our model, the elastic modulus E and density ρ can be obtained in terms of the equivalence of the axial and bending stiffness and gross weight, given by Eqs.(8) ~ (10).

$$EA = E_{s1}A_{s1} + E_cA_c + E_{s2}A_{s2} \tag{8}$$

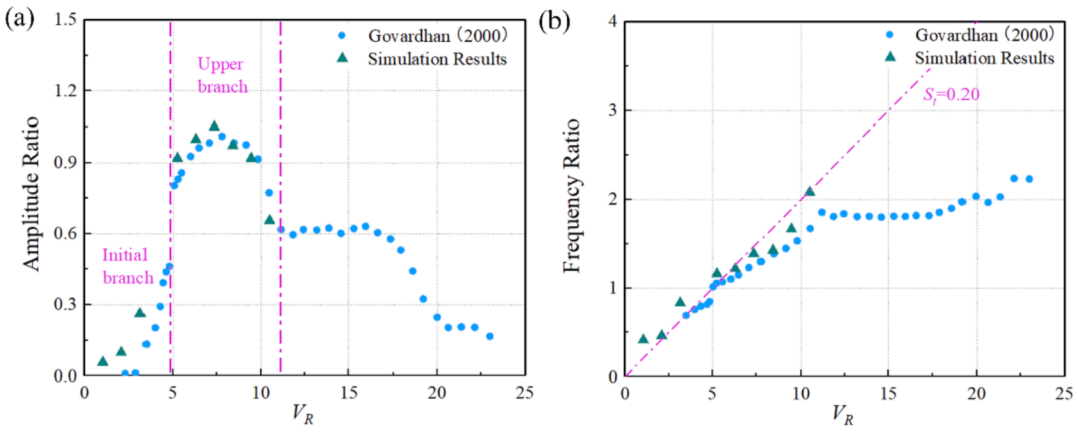

Fig. 4. Amplitude and frequency variation with reduced velocity for a low-mass-damping cylinder. S_t is Strouhal number.

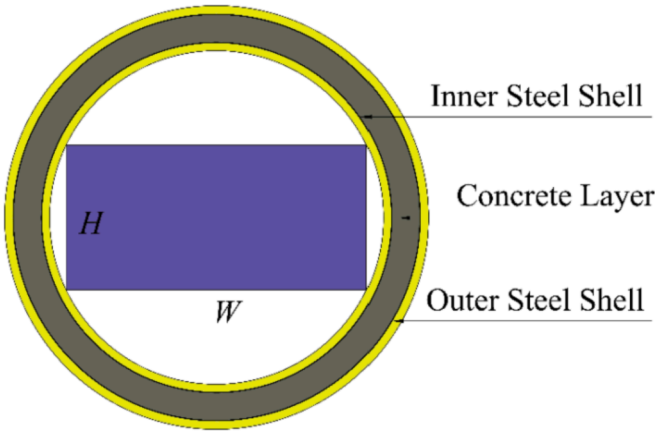

Fig. 5. SFT Steel shell concrete cross-section (the purple area represents the vehicle clearance zone).

$$EI = E_{s1}I_{s1} + E_cI_c + E_{s2}I_{s2} \tag{9}$$

$$\rho A = \rho_s(A_{s1} + A_{s2}) + \rho_c A_c \tag{10}$$

where E_{s1}, E_{s2}, E_c are the elastic modulus of outer shell, inner shell, and concrete, respectively; I_{s1}, I_{s2}, I_c are the cross-sectional moments of inertia of outer shell, inner shell, and concrete, respectively; A_{s1}, A_{s2}, A_c are the cross-sectional area of outer shell, inner shell, and concrete, respectively; ρ_s, ρ_c are the steel shell and concrete density, respectively; E, I, A, and ρ are the equivalent elastic modulus, moments of inertia, area, and density of the SSC structure, respectively. The material properties of the SFT tube can be seen in Table 4.

3.2.2. Parameters of SFT joint

Since the SFT tube may have a length of multiple kilometers, a monolithic tunnel tube cannot be cast due to issues with concrete cracking, transportation, and installation. Thus, tunnel segments or elements should be constructed, assembled, and connected with joints. The restrictions of the six degrees of freedom (DOFs) of the element joint should be accessed by the reliability and durability of the structure.

The allowable axial expansion-compression and water tightness properties need to be accounted for in the SFT joint design. With reference to immersed tunnels, Gina gasket and omega profiles designed to withstand axial loading and form water seals can be implemented. Gina gaskets are pre-compressed due to the water pressure and stiffened when further compressed, and are unstiffened when decompressed. The loading-compression behavior can be categorized into three regions by simplifying the curve of Fig. 6, where the initial axial stiffness k_0 is determined by the initial water pressure [42].

Table 4
Structure and material parameters.

Structure component	Parameter	Value
Tunnel tube	Total length (km)	20
	Element length (m)	100
	Young's modulus (GPa)	40.2
	Poisson's ratio (-)	0.18
	Structure dry density (kg/m^3)	2698
	Water density (kg/m^3)	1050
	Added mass coefficient (-)	1.0
	Damping ratio (-)	0.025
	Inner and outer shell thickness (mm)	16
	Tunnel wall thickness (m)	1.0
	Lateral clearance W (m)	11
	Vertical clearance H (m)	5
	Cross-sectional area of circular shape (m^2)	41.1
	Cross-sectional area of parametric shape (m^2)	43.8
Mooring line	Mooring interval (m)	100
	Nominal diameter (m)	0.18
	Mass/Unit length (kg/m)	644.7
	Added mass coefficient (-)	1.0
	Minimum breaking load (kN)	30689 (Grade R5)
Tunnel joint	Axial stiffness (GN/m)	22.1
	Shear stiffness (GN/m)	0.76
	Bending stiffness (GN m)	548
	Torsional stiffness (GN m)	592

The Gina gasket is modelled as one axial spring and two rotational springs (control the pitch and yaw motions) with axial stiffness k_u and bending stiffness k_θ. For a circular Gina gasket, stiffness can be obtained by Eqs. (11) and (12).

$$k_u = 2\pi k_0 r \tag{11}$$

$$k_\theta = \frac{M_{total}}{\theta} = \pi k_0 r^3 \tag{12}$$

where r is the circle radius of Gina gasket. A detailed derivation is in S1.

Transverse deformation of the joint should be restrained to avoid large displacements and leakage. With reference to immersed tunnels, shear forces in the joint can be transferred by shear keys, which can be applied as a basis for the SFT's joint design. The shear keys can be set uniformly on the outer or inner sides of the tunnel wall. The shear capacity of the joint is mainly determined by material property, wall thickness, and quantity, dimensions, and fabrication techniques of the shear keys. Torsional stiffness of the joint can also be provided by shear keys. The detail joint design including Gina gasket and shear keys can be

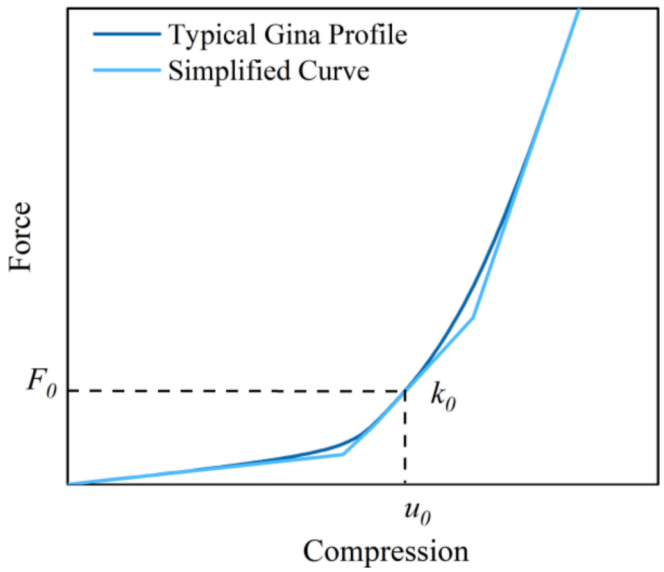

Fig. 6. Gina gasket loading-compressive behavior.

seen in Fig. 7

To access the shear key capacity of the joint for dynamic response modelling of the SFT, a three-dimensional FEM model consisting of two tunnel elements is established using LUSAS v15.2. Each element length is 100 m. Six shear keys with each dimension of 3 m × 0.6 m × 0.6 m are uniformly placed along the outer side of the wall (Fig. 8). The grid size of shear key and tunnel element is 0.1 m and 1 m, respectively. The tunnel elements and shear keys are modelled by the hexahedral volume element (TH4). The total nodes and elements in the model are 26052 and 18132, respectively. A rigid link constraint is applied to connect all the nodes on the shear keys (child nodes) with a center node (parent node), and hence, a unit vertical or torsional load can be added directly on the parent node. The effect of contact between surfaces of the two elements is simulated by a "slide-line" with a Coulomb friction coefficient of 0.2, and a close contact spring stiffness is adopted to soften the transition between in-contact and out-of-contact states. The material properties of the shear keys are equal to the tunnel element tube shown in Table 4. Accessories such as rubber pads are neglected in the model. Fig. 9 shows the shear stress distribution on each side of the joint under unit twisting and vertical load, respectively. It can be found that stress concentrates at the corners of the shear keys under the twisting load. Furthermore, larger shearing resistance is contributed by the horizontal shear keys compared with the vertical ones under the vertical load. By obtaining the maximum displacement of the shear keys in Table 5, the shear and torsional stiffness of the joint can therefore be estimated as 0.76 GN/m and 592 GN·m, respectively. Detailed joint properties composed by Gina gasket and shear keys are listed in Table 4. However, in engineering practice, the tunnel joint should be further assessed considering multiple factors such as mechanical properties, waterproofing, loading, construction technique, and maintainability.

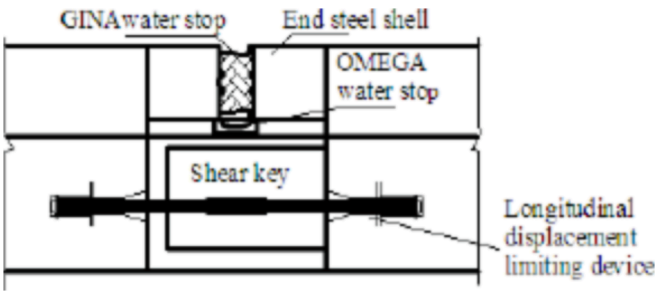

Fig. 7. Schematic drawing of the SFT joint design [43].

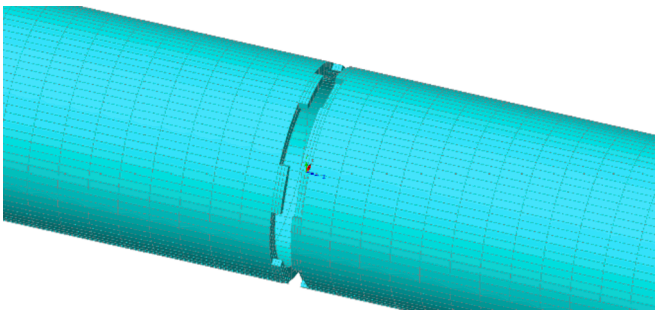

Fig. 8. FE mesh of shear keys applied in the model.

3.2.3. Numerical model setup

The characteristics of dynamic response of SFTs are complicated due to various types of hydrodynamic loads that the structure is exposed to and complex dynamic response of coupled components of tunnel tube, mooring lines, and tunnel joints. There is still no prototype SFT that has yet been built worldwide due to the immaturity of scientific research and technology. As one of potential SFT application sites, the Qiongzhou Strait, located between Hainan Island and the Leizhou Peninsula in the South China Sea (SCS), is applied for dynamic response analysis of the SFT in this study. The optimal SFT construction heading "*Line V*" (from Sitang in the Leizhou Peninsula to Tianwei in Haikou) is around 20 km width [5] (Fig. 10). Therefore, the overall length of the SFT tube in the example is 20 km, consisting of 200 tunnel elements. The mooring sets moored at mid-span of each tunnel element with an interval of 100 m. The submergence depth of the SFT is 40 m with a water depth of 100 m, and the variety of underwater terrain is neglected.

The software LUSAS v15.2 is employed to establish an SFT model coupling tube-joint-mooring components for the global dynamic response analysis (Fig. 11 (a)), where the tunnel tube with mooring lines is modeled by a "thick beam (BMS3)" element, and the tunnel element joint is modeled by a "Point joint (JSH4)" element. Each element joint is simulated in six DOFs including three force spring units (axial spring unit, horizontal shear spring unit, and vertical shear spring unit) and three torque spring units (torsional spring unit, bending spring unit in horizontal plane, and bending spring unit in vertical plane). Internal rigid constraints are implemented between the mooring line ends and the central mass of the SFT tube nodes. The mooring line ends are imposed rotational releases. Both ends of the tunnel tube are fixed. The mooring lines are arranged symmetrically composing 4 mooring lines in each set to balance restoring forces (Fig. 11 (b)). The basic parameters with respect to geometric and material properties of the SFT are summarized in Table 4. The environmental conditions are described in section 4 corresponding to each subsection.

In order to compare the FIV conditions and dynamic response of the SFT with different cross-section shapes, numerical models with two types of cross-section shapes (i.e., circular and parametric shapes shown in Fig. 12) are built up, respectively. The parametric shape is described by Bézier curves with the parameters combination of $b = 1.5$ m, $r = 0.5$ m, and $y_t = 4$ m. The definition of Bézier parameters can be found in our previous research [44,45]. Apart from the cross-sectional area, cross-sectional clearance and wall thickness, and structure and material parameters of the two numerical models are kept equal. The wet natural frequencies of the two numerical models are computed using LUSAS v15.2 and are listed in Table 6, and the obtained eigenmode shapes are presented in Fig. 13 (by exemplifying the parametric shape). Directions of excited motion of the first ten modes are consistent between the two models, but slightly larger natural frequencies for the circular shape are observed than for the parametric shape.

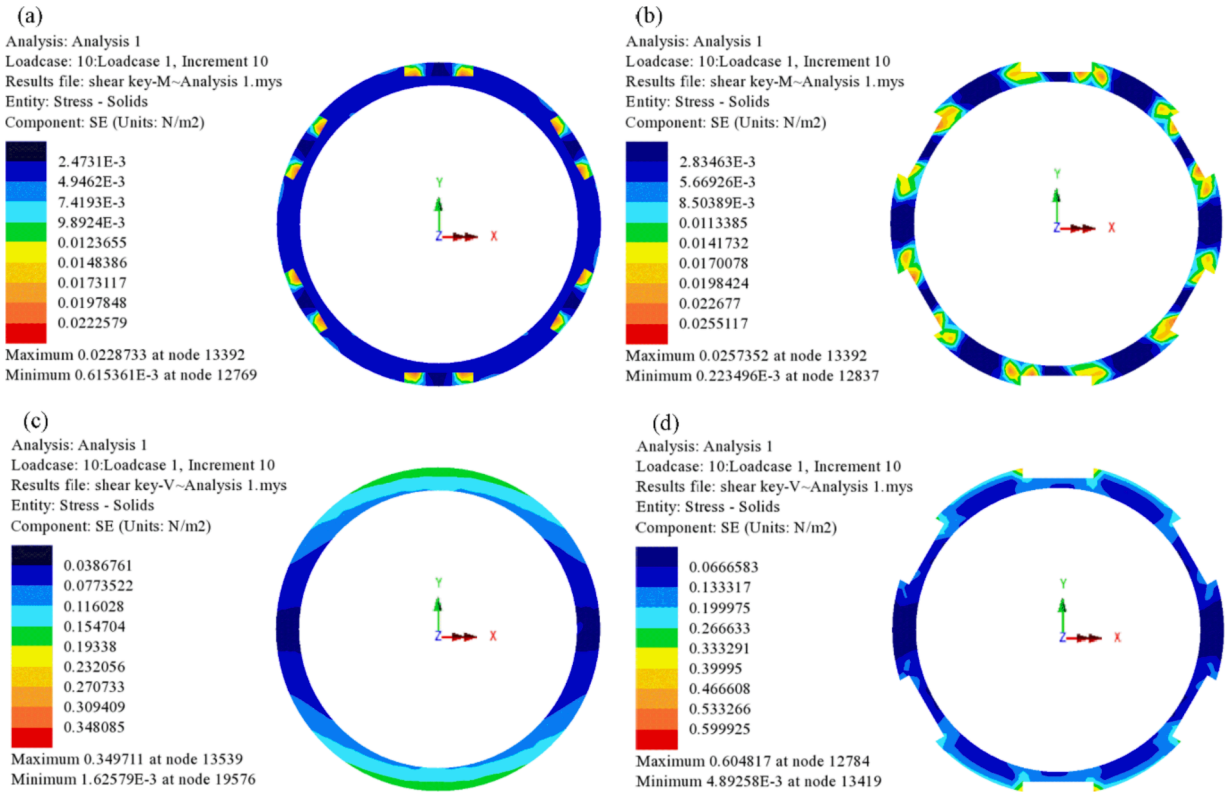

Fig. 9. (a, b) Stress contour under unit twisting load at the front and reverse side of the shear keys, respectively; (c, d) Stress contour under unit vertical load at the front and reverse side of the shear keys, respectively.

Table 5
Calculated results for shear keys.

Description	Value
Max. displacement of shear keys under unit vertical load	1.32×10^{-9} m
Max. displacement of shear keys under unit twisting load	1.69×10^{-12} rad

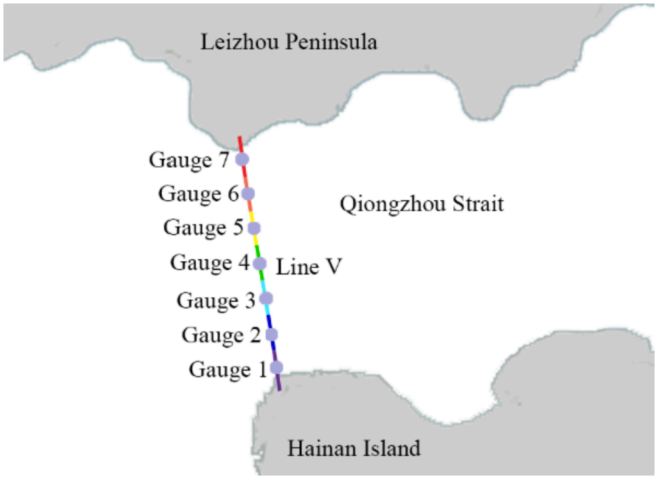

Fig. 10. The optimal heading for sea-crossing in the Qiongzhou Strait;, the virtual gauge described in section 4.3 are marked as grey dots, and the seven tube reaches are marked as lines in different colors.

4. FIV condition results

SFTs are subject to marine environmental conditions generally including currents, waves, and extreme events (e.g. tsunamis and typhoons). In order to investigate FIV of the SFT subject to different hydraulic loading, uniform current and regular wave induced forces are firstly calculated using the CFD code ANSYS Fluent v19.1. Furthermore, to examine the most severe conditions, an extreme event (a super typhoon example in the Qiongzhou Strait) is simulated by the large-scale oceanographic hydraulic modeling framework of Delft3D-FLOW coupled with the spectral wave model SWAN, and the small-scale hydrodynamic forcing on the structure is solved by the CFD code ANSYS Fluent v19.1. For a conservative computation, the hydraulic loading direction is calculated perpendicular to the longitudinal direction of the SFT. Finally, a coupled tube-joint-mooring SFT model is computed using FEM in the time-domain for the global dynamic response analysis accordingly.

4.1. FIV conditions under currents

The velocity fields and hydrodynamic forcing on two types of cross-sections (i.e., circular and parametric shapes) with a current speed of 1.5 m/s solved by the CFD code ANSYS Fluent v19.1 are shown in Fig. 14. It can be seen that the parametric shape experiences flow separation further downstream and has a smaller wake region than the circular cross section due to its more streamlined geometry (Fig. 14 (a) and (b)). The circular shape exhibits a classical '2S' vortex formation mode (characterized by two single vortices shedding per oscillation cycle), corresponding to the so-called "initial branch" sequence. Furthermore, the drag is over ten times smaller for the parametric shape than the circular shape (Fig. 14(c)). Since no apparent vortex pattern can be observed with the parametric shape, the drag and lift forces on the SFT are thereby effectively mitigated.

To compare dynamic response of the SFTs with the two cross-section shapes under current conditions, firstly, uniform current speeds varying from 0.5 m/s to 1.5 m/s at 0.25 m/s intervals are selected based on practical hydraulic conditions; subsequently, the stable (after model

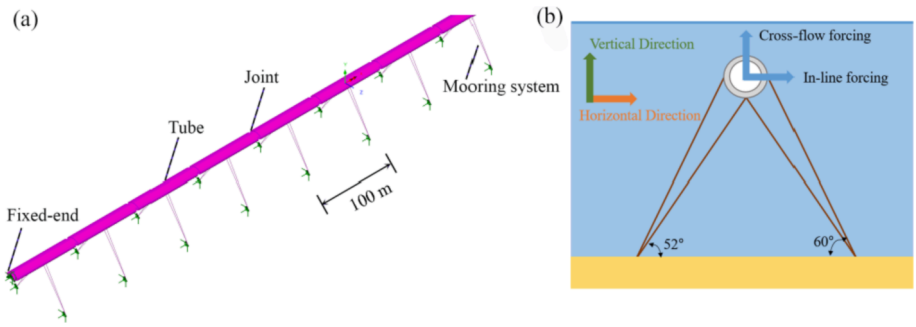

Fig. 11. The SFT model; (a) Coupled tube-joint-mooring system FEM model (Part of the model); (b) Mooring lines arrangement.

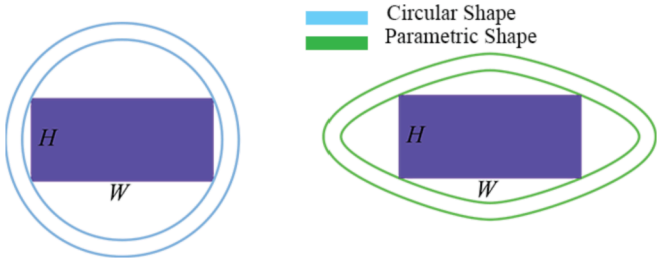

Fig. 12. SFT cross-section shapes.

Table 6
Wet natural frequencies of the SFT tube for different cross-section shapes.

Mode number	Wet natural frequency f_n (Hz)		Direction
	Circular shape	Parametric shape	
1	0.129	0.123	Horizontal
2	0.133	0.127	Horizontal
3	0.139	0.130	Horizontal
4	0.139	0.137	Axial
5	0.146	0.138	Horizontal
6	0.153	0.143	Horizontal
7	0.160	0.150	Horizontal
8	0.166	0.156	Horizontal
9	0.172	0.162	Horizontal
10	0.176	0.166	Horizontal

spin-up) hydrodynamic forcing on the two types of cross-sections under each current speed is computed by CFD; finally, the calculated hydrodynamic forcing in the time-domain is used as the hydraulic load acting on each tunnel element node of the FEM structural model with the corresponding shape for structural dynamic analysis.

A comparison of the envelopes of the tube displacement at different current speeds between the circular shape and the parametric shape is seen in Fig. 15 (to prevent clutter, only current speeds of 0.50 m/s, 1.00 m/s, and 1.50 m/s are shown). In the inline (IL) direction, the displacement of the tube with circular shape is ten times larger than with the parametric shape (Fig. 15 (a)), which concurs with the magnitude of the drag (Fig. 14 (c)). In the cross-flow (CF) direction, the displacement of the tube with circular shape is thirty times larger than that of the parametric shape case (Fig. 15 (b)), indicating the displacement of the SFT tube can be effectively reduced by adopting the parametric cross-section. The tube displacement in the IL direction are larger than that in the CF direction, indicating the in-line forcing has a major impact on the structural dynamics. Note that the it is unlikely to induce large displacements of the SFT tube under steady currents, similar to what was seen by prior work [46,47].

The relation of maximum IL displacement of the tube with different cross-sectional shapes to V_R is shown in Fig. 16. The displacement increases with increasing current speed. The maximum IL displacement is approximately linearly correlated with V_R, with a slope of 0.150 m for the circular shape and 0.020 m for the parametric shape. Chen et al. [12] found that the "lock-in" phenomenon for the SFT system under steady current conditions occurs at $V_R = 5$. Govardhan and Williamson [39] found that the largest VIV response for a cylinder with a small mass ratio occurs at $V_R = 8$. It is clear that the V_R values in our models are far away from the lock-in regime and the "upper branch" (characterized by a notable jump in the vortex phase), making resonance between vortex shedding and the dynamic response of the SFT tube unlikely. In this case, to reduce computational load, the static analysis is suggested to be conducted. However, if the mooring stiffness is not sufficient or the current speed is high enough, the vortex shedding frequency can overlap with the natural frequencies of the SFT. In that case, dynamic analysis is essential. However, for thin mooring cables, V_R can vary over a wide range and may overlap the lock-in region.

4.2. FIV conditions under waves

In order to evaluate dynamic response of different cross-section shapes of the SFT tube under wave forcing, measured wave data in the Qiongzhou Strait is used [48] (Table 7). Fig. 17 compares the computed stable (after model spin-up) wave load calculated using CFD, acting on the two shapes for waves with a return period of 20 years The parametric shape experiences a smaller in-line force due to its smaller characteristic length than that of the circular shape.

A comparison of the envelopes of the tube displacements at different wave conditions between the circular shape and the parametric shape is seen in Fig. 18.The maximum IL displacement reaches 2.7 m at a return period of 20 years because the wave frequency is close to the first mode structural frequency (IL direction) of the SFT tube with the circular shape. The maximum CF displacement is 0.2 m at a return period of 100 years with the parametric shape, and the displacement remains nearly constant along the span. The CF displacement for the parametric shape is larger than for the circular shape; this is consistent with the forcing distribution. The reduction of the tube stiffness with the parametric shape (due to a large cross-section area) also incurs an increase of displacement in the CF direction. Again, it proves that the tube displacements in the IL direction are much larger than that in the CF direction, making reduction of the in-line force more important than the force in CF direction. Since the parametric shape has a smaller IL displacement, its hydrodynamic performance is preferable to that of the circular shape. It should be noted that in actual engineering practice, the SFT cross-section design should also consider the combined effects of the hydrodynamic characteristics, structure behavior, technical difficulties, service level, and construction cost.

To better comprehend the impacts of the wave parameters on the FIV, a sensitivity analysis of wave height and period is carried out. Considering it was proved that the structural displacement increases with increasing wave height (wave load is approximately proportional to wave height) [49], and the displacement in the CF direction is comparatively small, we explore how wave period affects only the IL

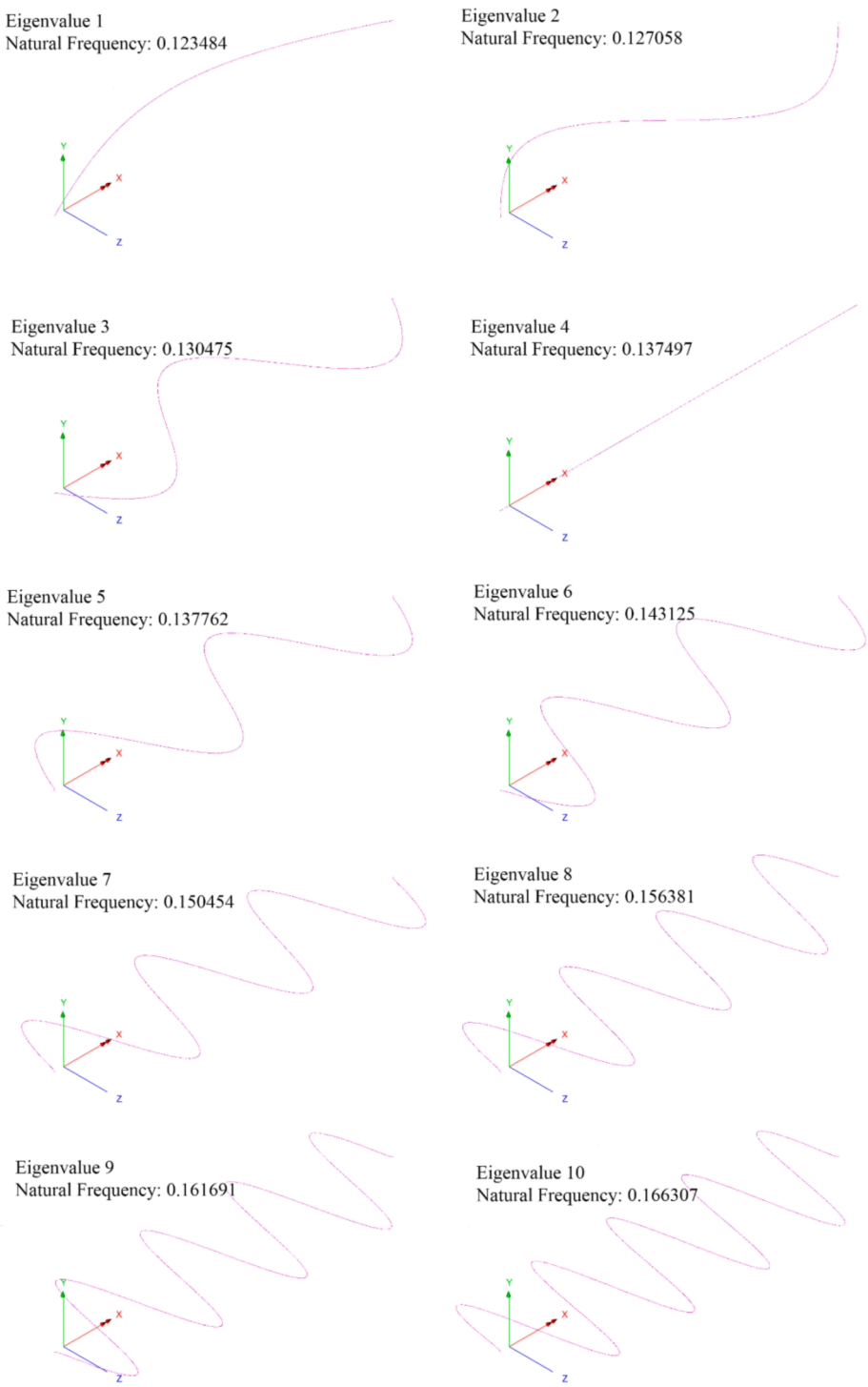

Fig. 13. Numerical eigenmode shapes of the SFT with the parametric shape cross-section. Frequency in Hz.

displacement of the SFT tube with the parametric shape. A fixed wave height of 7 m with wave periods of 7.6 s, 7.2 s, 6.8 s, 6.4 s, and 6.0 s are selected.

Fig. 19 shows the envelopes of the tube IL displacements under various wave periods. As the deflected shape of the tube reflects the mode of excitation, a single dominant vibration mode is presented at each wave period of 7.2 s, 6.4 s, and 6 s. The corresponding horizontal vibration modes are the fifth mode, the seventh mode, and the eleventh mode, respectively. However, multiple dominant vibration modes exist at wave periods of 7.6 s and 6.8 s, due to the irregularity of the oscillation shapes. It can be found that with decreasing wave period, higher vibration modes are excited, but the maximum tube displacement doesn't show positive correlation with wave period. The case of wave period of 7.2 s illustrates a larger dynamic response than $T = 7.6$ s, and the case of $T = 6.4$ s has the same maximum displacement as $T = 6.8$ s. It can be concluded that a single-mode dominant vibration, to a certain extent, amplifies structural displacement compared with multi-mode vibration. As per Kunisu [50], the wave force acting on the SFT is strongly dependent on wave number (proportional to wave period). Firstly, the wave force increases dramatically with increasing wave number and after achieving a peak value at a certain wave number, force decreases slowly with increasing wave number. Therefore, the

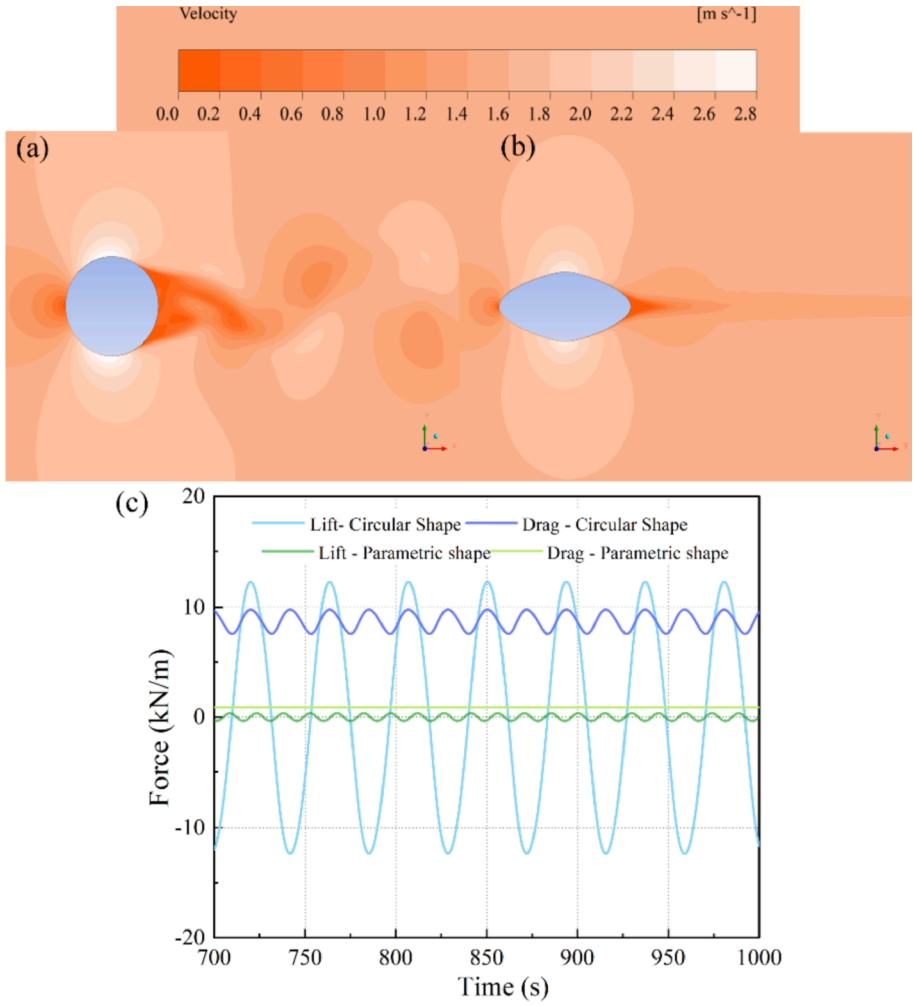

Fig. 14. (a) Instantaneous flow velocity contour for the circular shape; (b) Sequential flow velocity contour for the parametric shape; (c) Drag and lift time-history for the two shapes at $V = 1.5$ m/s.

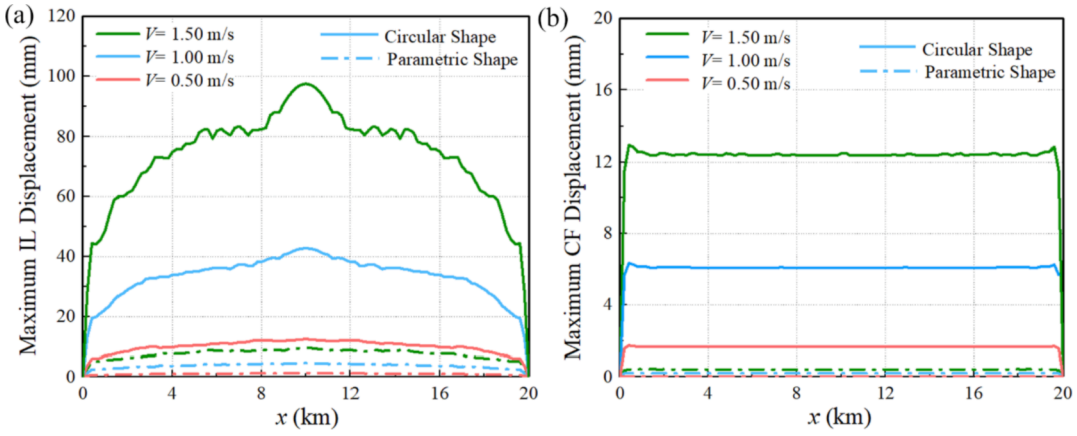

Fig. 15. (a, b) Envelopes of the IL and CF displacements under steady currents for different shapes.

maximum displacement at $T = 7.6$ s is smaller than at $T = 7.2$ s and it decreases remarkably for wave periods lower than 7.2 s.

In order to further demonstrate the excited modes at different wave periods and determine the dominant modes explicitly, time series of IL displacement along the entire span, and the corresponding frequency spectrum at mid-span, are depicted in Fig. 20. The vibration frequency spectra are attained by employing a fast Fourier transform (FFT). A fifth mode standing wave pattern is seen at $T = 7.2$ s in Fig. 20 (a). Meanwhile, a single dominant vibration frequency associated with the fifth mode in the horizontal plane (0.143 Hz), followed by a weak spectral peak from the first mode (0.123 Hz), is observed in Fig. 20 (b). However, at $T = 7.6$ s, two dominant vibration modes with similar modal weights are seen in Fig. 20 (d). The third mode (0.130 Hz) appreciably overlaps the first mode (0.123 Hz), and both vibration modes contribute to the

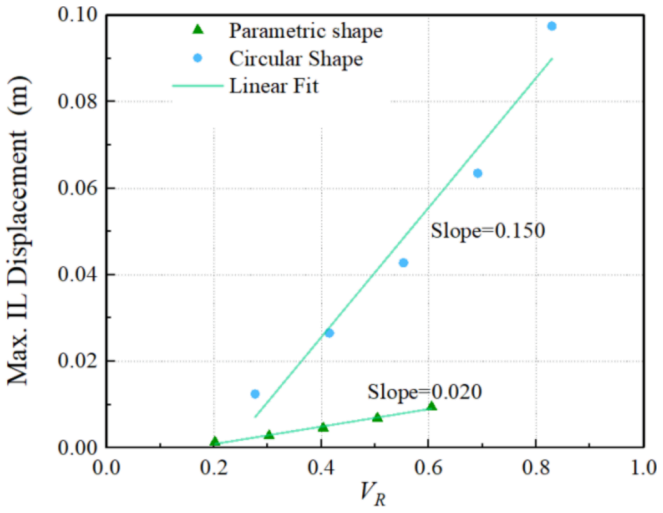

Fig. 16. The maximum IL displacement of the tube versus the reduced velocity.

Table 7
Measured data for extreme wave conditions in the Qiongzhou Strait, from [43].

Return Period (year)	Wave Height (m)	Wave Length (m)
20	7.0	115.11
25	7.3	119.45
100	8.6	137.38

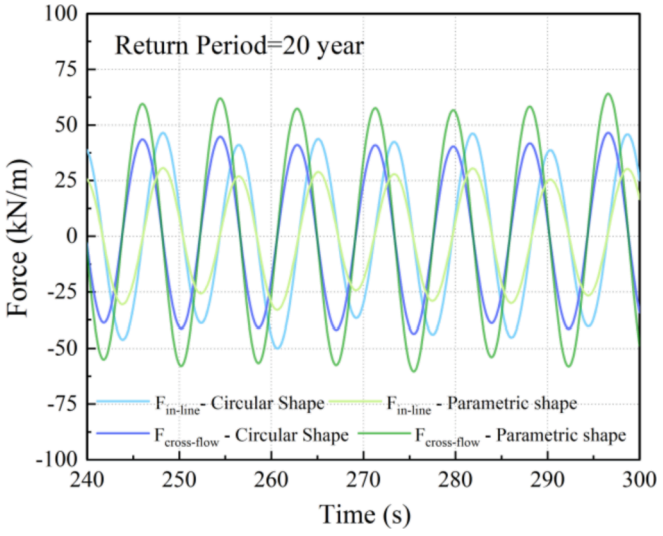

Fig. 17. Wave force time-history of the two shapes with a wave return period of 20-years.

dynamic behavior of the SFT tube (Fig. 20 (c)). It can be further verified by Fig. 13 and Fig. 19 that the deflected shape of the tube at $T = 7.6$ s is mainly composed of a third mode superposed with a first mode. Compared with steady current conditions, unlike the generally current-dominated situation of risers, FIV of the SFT tube is more critical under wave conditions due to its large cross-section. Wave effects on the SFT are remarkable and complex, particularly for single dominant mode excitations.

4.3. Dynamic response of the SFT under extreme events

Our previous research regarding the impacts of the extreme events on the SFT showed that storm surge is more devastating than tsunami in the Qiongzhou Strait [28]. Therefore, as the most powerful and strongest typhoon to make landfall on Hainan Island since 1949, super typhoon Rammasun (2014) was selected as an extreme event for hydrodynamic assessment of the SFT. Rammasun made first landfall on Wenchang, Hainan at 7:00 UTC on July 18, 2014, and dissipated when it made its second landfall in Guangxi province on July 19. We evenly placed seven virtual gauges along the optimal SFT heading ("*Line V*") to obtain the hydrodynamic conditions in the Qiongzhou Strait (Fig. 10). Therefore, the 20 km long SFT tube is divided into seven tube reaches, and the hydraulic loading on each reach is taken as the loading measured at the corresponding virtual gauge. The tube reach length is 2.5 km at Gauges 2–6 and 3.75 km at Gauges 1 and 7.

In order to consider spatiotemporal variation and randomness of hydraulic loading (typhoon-induced waves) along the tunnel span, a large-scale oceanographic model in the far-field was established by means of coupling the integrated atmosphere–ocean framework of Delft3D-FLOW and SWAN. The hydrodynamic model computational time step is 1 s and is coupled with a stationary SWAN wave simulation every 60 min. Wind stress and tidal forcing drive the simulation from 0:00 on July 14 to 0:00 on July 20, 2014. Detailed model settings and typhoon track data can be found in [28]. Time series of wave height are determined by the along strait component of wave energy flux and the corresponding wave period at each virtual gauge, which were extracted from the model as shown in Fig. 21. It can be observed that the maximum wave height at each virtual gauge occurs at 14:00 on July 18 as the typhoon eye enters the strait. Therefore, for a conservative consideration, the maximum wave height and the corresponding wave period at each virtual gauge are adopted for small-scale hydrodynamic forcing simulation. The wave force on the SFT at each virtual gauge location (force per meter) is solved by a two-dimensional flow strip using the CFD code ANSYS Fluent v19.1. The wave force on each tube reach is solved by integrating the hydraulic loading (force per meter) at the corresponding virtual gauge along the reach. Therefore, the spatio-temporally varying wave force on the super long tunnel tube can be properly considered by spatially varying the hydraulic loading on different tube reaches in the time-domain.

The global dynamic response of the coupled tube-joint-mooring SFT model under this extreme event is analyzed using LUSAS v15.2 in the time-domain. According to sections 4.1 and 4.2, the SFT tube with the parametric shape has preferable dynamic response properties under both current and wave conditions. Therefore, the global dynamic response of the SFT is assessed for the parametric shape.

Fig. 22 shows time series of IL displacement along the full span of the SFT tube and the corresponding frequency spectrum at tube mid-span under the extreme event. From Fig. 22 (a), the evolution of the oscillation pattern indicates the tube vibration at the region of heavy loading transferring its energy to the other side to maintain motion via traveling wave patterns, as the wave loading is more severe near Gauge 1 ($x = 0$) than Gauge 7 ($x = 20$ km) (Fig. 10). The IL response shows a pronounced standing wave characteristic at $x = 0$ due to reflection at the boundary. However, the oscillation pattern distribution shows irregularity, and the energy propagation process is complex, owing to multi-mode sharing and interaction. Several peak vibration frequencies overlapping and sharing modes can be observed in Fig. 22 (b). The space–time varying hydraulic loading along the tube span is notably accounted for the modal interactions.

Fig. 23 shows the envelopes of the IL displacement and internal forces on the SFT along the span under the extreme event. The displacement, acceleration, and internal forcing in the horizontal direction are much larger than in the vertical direction. The maximum displacement, acceleration and shear force reach 0.28 m, 0.36 m/s^2, and 4.6 MN at $x = 5.7$ km, respectively. The torque is much larger than the bending moment which reaches the maximum value of 280 MN m at $x = 4.9$ m. The forcing variation along the span may cause fatigue damage to the joints. Since both ends are assumed to be fixed in the simulation, excessive internal forcing due to torque and bending moment may cause

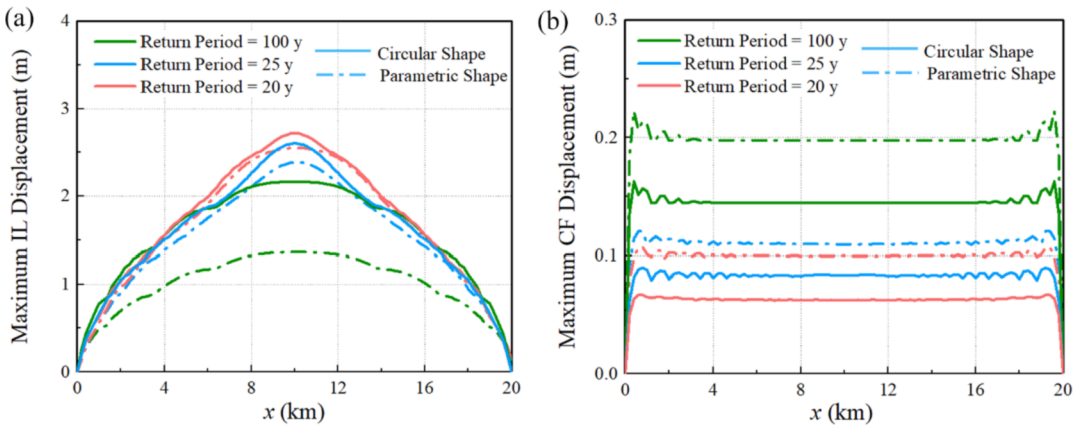

Fig. 18. (a, b) Envelopes of IL and CF structural displacements under waves.

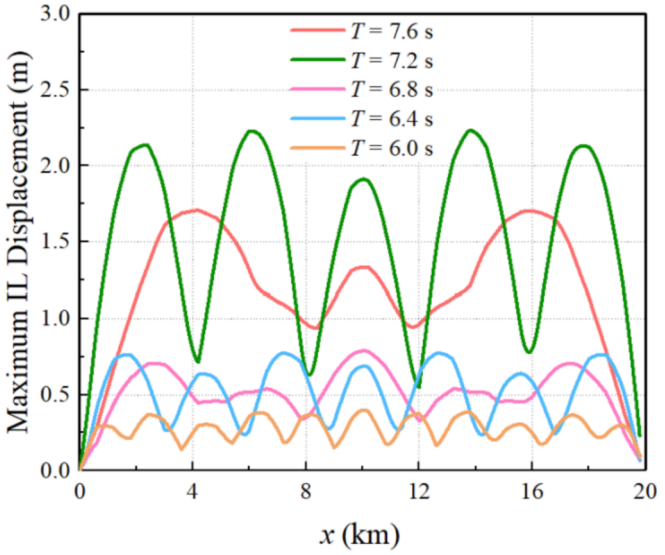

Fig. 19. Envelopes of the IL displacements for various wave periods.

structure fatigue and buckling damage at the shore connections. In this case, elastic bearings, bi-linear elastic bearings, and passive isolation bearings can be incorporated as options for the shore connections [51]. An intermediate flex joint allowing axial deformation such as a telescopic joint or stroke-out-of-slip joint as applied in marine risers can also be utilized in the SFT shore connection design [52]. However, investigation of shore connection type and its effects on dynamic response of the SFT are not within the scope of this research.

5. Conclusion

In this paper, a conceptual engineering study for the SFT's application is provided by using ANSYS Fluent v19.1 and LUSAS v15.2. The use of full CFD allowed VIV prediction, which the previous publications neglected due to their use of a potential flow model [13,14] instead of CFD. Our model of the SFT as a system of rigid segments connected by flexible joints with shear keys and Gina gaskets also allows more realistic simulation of dynamic behavior than previous works resolved. A pragmatic one-way FSI approach consisting of a multi-scale cascade of hydrodynamic models combined with FEM are proposed to consider the spatiotemporal variation and randomness of hydrodynamic loading. Steel shell concrete composite material is proposed for the SFT tube, and stiffness properties of a tunnel joint composed of a Gina gasket and shear keys are quantified. A prototype super long and large aspect ratio SFT numerical model composed of a coupled tube-joint-mooring system is established for FIV prediction and global dynamic response analysis in the time-domain. The dynamic response and FIV predictions of an SFT with parametric and a circular cross section shapes are compared under steady currents and waves. The main conclusions are briefly summarized as follows:

(1) The spatiotemporal variation and randomness of hydraulic loading can be effectively solved by multi-scale models including a large-scale oceanographic (shallow water equation) model and a small-scale hydrodynamic forcing (CFD) model.

(2) The SFT tube is unlikely to experience strong resonance under steady currents, due to its large cross-section dimension.

(3) FIV of the SFT tube is mainly dominated by wave conditions. Wave effects on FIV of the SFT are complex. A single dominant mode excitation of the tube with a large wave height and period should be avoided.

(4) An SFT with a parametric cross-section shape is recommended over the simpler circular shape due to the effectively reduced hydrodynamic forcing and structural dynamic response of the parametric cross-section.

(5) In an extreme event, standing and traveling wave patterns of the tube oscillation can be observed due to multi-mode sharing and interaction. The forcing variation along the span may cause fatigue damage to the joints, and the excessive internal forcing due to torque and bending moment may cause structure fatigue and buckling damage at the shore connections.

In spite of these achievements for the FIV prediction and dynamic response analysis of the SFT, some restrictions and future work still should be noted in this study

(1) Flow-induced vibration conditions are studied under uniform currents and regular waves. In reality, the SFT will be subject to inhomogeneous irregular waves and unsteady currents. Therefore as a future step, the dynamic response of the SFT should also be examined based on such realistic environmental conditions.

(2) Hydraulic loading computation based on the framework of two-dimensional flow strips conserves computational resources, but is limited by incapability of accounting for complex three-dimensional effects, axial pressure gradients, or oblique flows.

(3) Hydrodynamics of the SFT is a multi-physics issue with a strong interaction between the flow field and tunnel tube. It is rational to assume the flow is not heavily affected by small structural deformations of an SFT at this stage. However, the importance of this effect should be quantified in future research.

CRediT authorship contribution statement

P.X. Zou: Conceptualization, Methodology, Software, Validation, Data curation, Visualization, Writing – original draft. **Jeremy D.**

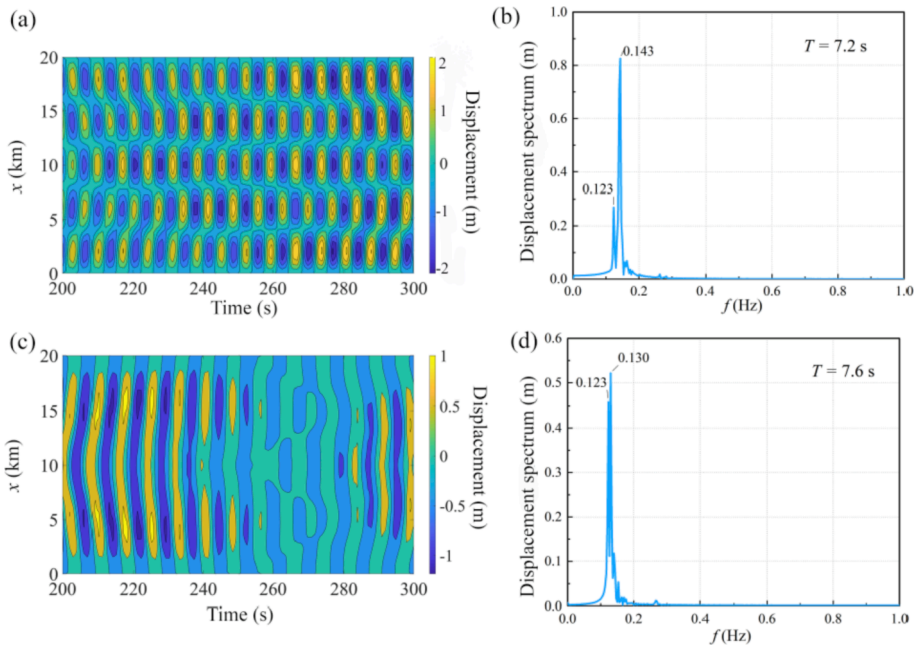

Fig. 20. (a, b) Time series of IL displacement along the entire span, and mid-span frequency spectrum at $T = 7.2$ s; (c, d) Time series of IL displacement along the entire span, and mid-span frequency spectrum at $T = 7.6$ s.

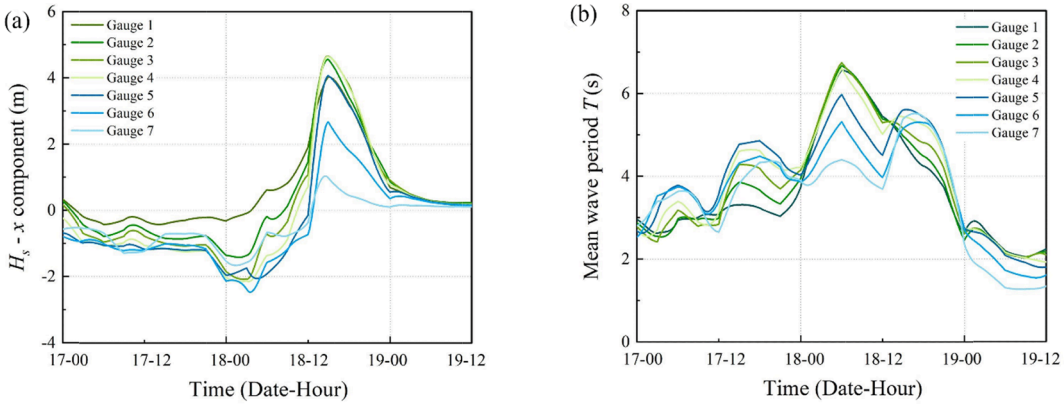

Fig. 21. (a) Wave heights corresponding to along-strait components of orbital velocity vectors at the seven virtual gauges; (b) The corresponding wave periods at the seven virtual gauges.

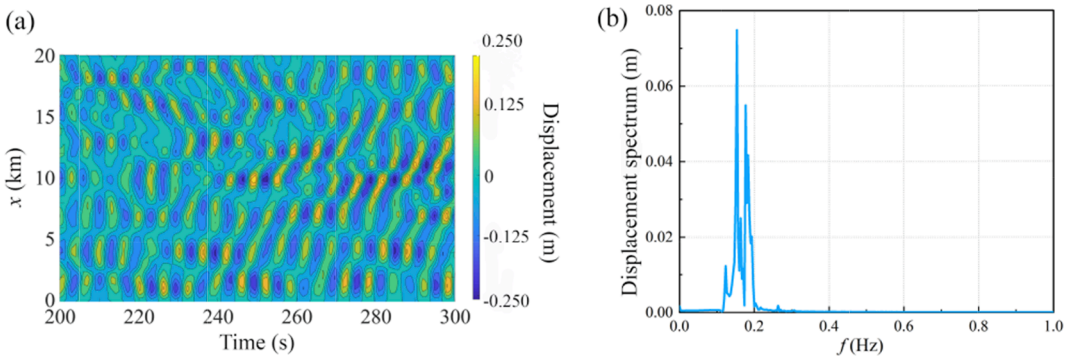

Fig. 22. (a) The spatiotemporal IL displacement under extreme events; (b) mid-span vibration frequency spectrum under extreme events.

Bricker: Conceptualization, Methodology, Writing – review & editing, Supervision. **L.Z. Chen:** Methodology, Writing – review & editing. **Wim S.J. Uijttewaal:** Writing – review & editing, Supervision. **Carlos Simao Ferreira:** Writing – review & editing.

Declaration of Competing Interest

The authors declare that they have no known competing financial interests or personal relationships that could have appeared to influence

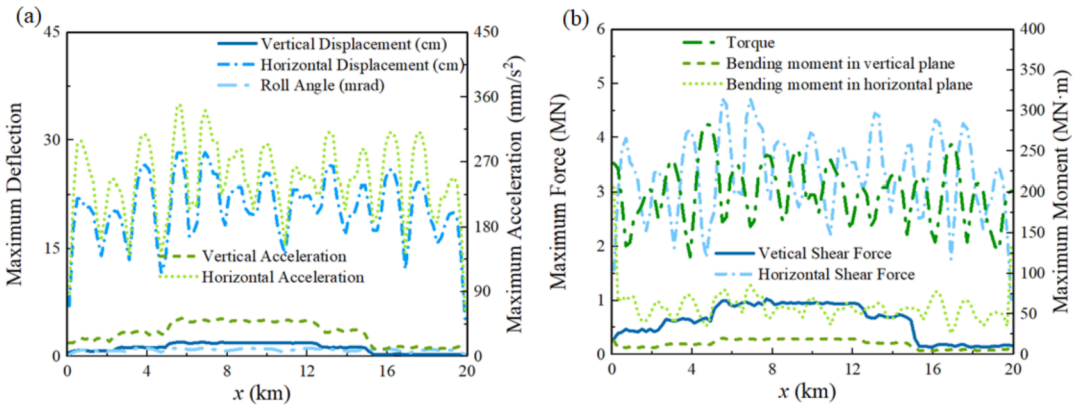

Fig. 23. (a) Envelopes of the IL displacement under the extreme event; (b) Envelopes of internal forces under the extreme event.

the work reported in this paper.

Acknowledgement

The study presented in this paper was conducted in the submerged floating tunnel research project funded by China Communications Construction Company Ltd. (CCCC) .

Appendix A. Supplementary material

Supplementary data to this article can be found online at https://doi.org/10.1016/j.engstruct.2021.113809.

References

[1] Zou PX, Bricker JD, Uijttewaal WSJ. The impacts of internal solitary waves on a submerged floating tunnel. Ocean Eng. 2021;238:109762.
[2] Remseth S, Leira BJ, Okstad KM, Mathisen KM, Haukås T. Dynamic response and fluid/structure interaction of submerged floating tunnels. Comput. Struct. 1999;72(4):659–85. https://doi.org/10.1016/S0045-7949(98)00329-0.
[3] Larssen RM, Jakobsen SE. Submerged floating tunnels for crossing of wide and deep fjords. Procedia Eng 2010;4:171–8. https://doi.org/10.1016/j.proeng.2010.08.020.
[4] Martire G, Faggiano B, Mazzolani FM, Zollo A, Stabile TA. Seismic analysis of a SFT solution for the Messina Strait crossing. Procedia Eng 2010;4:303–10. https://doi.org/10.1016/j.proeng.2010.08.034.
[5] Yan H, Zhang F, Yu J. The lectotype optimization study on submerged floating tunnel based delphi method. Procedia Eng 2016;166:118–26. https://doi.org/10.1016/j.proeng.2016.11.574.
[6] Deng S, Ren H, Xu Y, Fu S, Moan T, Gao Z. Experimental study of vortex-induced vibration of a twin-tube submerged floating tunnel segment model. J. Fluids Struct. 2020;94:102908. https://doi.org/10.1016/j.jfluidstructs.2020.102908.
[7] Yang Z, Zhang H, Li J, Yuan C, Ji X. A study on the wave-current-induced motion responses of submerged floating tunnels using longitudinal truncated model tests. Ocean Eng. 2021;39:44–52. in Chinese.
[8] Kamphuis JW. Hydrodynamics around cylindrical structures. Coast. Eng. 1998;33(1):69. https://doi.org/10.1016/S0378-3839(97)00031-8.
[9] Liu G, Li H, Qiu Z, Leng D, Li Z, Li W. A mini review of recent progress on vortex-induced vibrations of marine risers. Ocean Eng 2020;195:106704. https://doi.org/10.1016/j.oceaneng.2019.106704.
[10] Felisita A, Gudmestad OT, Karunakaran D, Martinsen LO. A review of VIV responses of steel lazy wave riser. In: Proceedings of the International Conference on Offshore Mechanics and Arctic Engineering -; 2016. https://doi.org/10.1115/OMAE2016-54321.
[11] Wu X, Ge F, Hong Y. A review of recent studies on vortex-induced vibrations of long slender cylinders. J. Fluids Struct. 2012;28:292–308. https://doi.org/10.1016/j.jfluidstructs.2011.11.010.
[12] Chen Z, Xiang Y, Lin H, Yang Y. Coupled vibration analysis of submerged floating tunnel system in wave and current. Appl. Sci. 2018;8(8):1311. https://doi.org/10.3390/app8081311.
[13] Mai J, Yang X, Guan B. Dynamic response analysis of the submerged floating tunnel subjected to the wave and current. J. Hydrodyn. Ser. A 2005;20:616–23 (in Chinese).
[14] J.T. Mai, X.C. Yang, B.S. Guan, Response analysis of the submerged floating tunnel subjected to waves and currents, Tiedao Xuebao/Journal China Railw. Soc., vol. 30, no. 2, 2008 (in Chinese).
[15] Hong Y, Ge F. Dynamic response and structural integrity of submerged floating tunnel due to hydrodynamic load and accidental load. Procedia Eng 2010;4:35–50. https://doi.org/10.1016/j.proeng.2010.08.006.
[16] Wu X, Ge F, Hong Y. Effect of travelling wave on vortex-induced vibrations of submerged floating tunnel tethers. Procedia Eng 2010;4:153–60. https://doi.org/10.1016/j.proeng.2010.08.018.
[17] E. Passano, C.M. Larsen, H. Lie, J. Wu, VIVANA theory manual, Nor. Mar. Technol. Res. Inst. Trondheim, Norway. Curr. profiles with High. Veloc. Prod. high damage both riser's Up. catenary buoyancy Sect. due to high Curr. Expo. shallower water depth high c, 2014.
[18] Vandiver JK, Li L. Shear7 V4. 4 program theoretical manual. Massachusetts Inst. Technol. 2005.
[19] Chen W, Li Y, Fu Y, Guo S. On mode competition during VIVs of flexible SFT's flexible cylindrical body experiencing lineally sheared current. Procedia Eng 2016;166:190–201. https://doi.org/10.1016/j.proeng.2016.11.582.
[20] Zhang Y, Habashi WG, Khurram RA. Predicting wind-induced vibrations of high-rise buildings using unsteady CFD and modal analysis. J. Wind Eng. Ind. Aerodyn. 2015;136:165–79. https://doi.org/10.1016/j.jweia.2014.11.008.
[21] Ulveseter JV, Thorsen MJ, Sævik S, Larsen CM. Time domain simulation of riser VIV in current and irregular waves. Mar. Struct. 2018;60:241–60. https://doi.org/10.1016/j.marstruc.2018.04.001.
[22] Chen W, Li M, Zhang L, Tan T. Study on multimode vortex-induced vibration of deepwater riser in different flow fields by finite element simulations. J. Offshore Mech. Arct. Eng. 2016. https://doi.org/10.1115/1.4031729.
[23] Wijesooriya K, Mohotti D, Amin A, Chauhan K. Comparison between an uncoupled one-way and two-way fluid structure interaction simulation on a super-tall slender structure. Eng Struct 2021;229:111636. https://doi.org/10.1016/j.engstruct.2020.111636.
[24] Benra F-K, Dohmen HJ, Pei Ji, Schuster S, Wan Bo. A comparison of one-way and two-way coupling methods for numerical analysis of fluid-structure interactions. J. Appl. Math. 2011;2011:1–16. https://doi.org/10.1155/2011/853560.
[25] D. Hydraulics, Delft3D-FLOW user manual, Delft, the Netherlands, 2006.
[26] Duanmu Yu, Zou Lu, Wan D. Numerical analysis of multi-modal vibrations of a vertical riser in step currents. Ocean Eng. 2018;152:428–42. https://doi.org/10.1016/j.oceaneng.2017.12.033.
[27] Lin Ke, Wang J. Numerical simulation of vortex-induced vibration of long flexible risers using a SDVM-FEM coupled method. Ocean Eng. 2019;172:468–86. https://doi.org/10.1016/j.oceaneng.2018.12.006.
[28] Zou PX, Bricker JD, Uijttewaal WSJ. Impacts of extreme events on hydrodynamic characteristics of a submerged floating tunnel. Ocean Eng. 2020;218:108221. https://doi.org/10.1016/j.oceaneng.2020.108221.
[29] Roeber V, Bricker JD. Destructive tsunami-like wave generated by surf beat over a coral reef during Typhoon Haiyan. Nat. Commun. 2015;6(1). https://doi.org/10.1038/ncomms8854.
[30] Lin H, Xiang Y, Yang Y. Vehicle-tunnel coupled vibration analysis of submerged floating tunnel due to tether parametric excitation. Mar. Struct. 2019;67:102646. https://doi.org/10.1016/j.marstruc.2019.102646.
[31] C. Jin, J. M.-H. Kim, J. Choi, and W.-S. Park, Coupled Dynamics Simulation of Submerged Floating Tunnel for Various System Parameters and Wave Conditions, 2018, doi: 10.1115/omae2018-78687.
[32] F. ANSYS, ANSYS fluent theory guide 19.1, ANSYS, Canonsburg, PA, 2019.
[33] Zou P, Bricker JD, Uijttewaal W. Submerged floating tunnel cross-section analysis using a transition turbulence model. J. Hydraul. Res. 2021. https://doi.org/10.1080/00221686.2021.1944921.
[34] Tariverdilo S, Mirzapour J, Shahmardani M, Shabani R, Gheyretmand C. Vibration of submerged floating tunnels due to moving loads. Appl. Math. Model. 2011;35(11):5413–25. https://doi.org/10.1016/j.apm.2011.04.038.
[35] F. E. A. LTD, "LUSAS user manual." Version.
[36] Liu M, Gorman DG. Formulation of Rayleigh damping and its extensions. Comput Struct 1995;57(2):277–85.
[37] Cruz C, Miranda E. Evaluation of the Rayleigh damping model for buildings. Eng. Struct. 2017;138:324–36. https://doi.org/10.1016/j.engstruct.2017.02.001.
[38] O. Manual, Version 9.8 b, Orcina Ltd, 2014.
[39] Govardhan R, Williamson CHK. Modes of vortex formation and frequency response of a freely vibrating cylinder. J. Fluid Mech. 2000;420:85–130. https://doi.org/10.1017/S0022112000001233.

[40] Kimura H, Moritaka H, Kojima I. Development of sandwich-structure submerged tunnel tube production method. Nippon Steel Tech. Rep. 2002.
[41] Li Y, Song S, Liu Y. Steel web effects on shear mechanism of steel shell-concrete composite structure. Eng. Struct. 2020;225:111258. https://doi.org/10.1016/j.engstruct.2020.111258.
[42] R.S. Van Oorsouw, Behaviour of segment joints in immersed tunnels under seismic loading, 2010.
[43] Zhang K, Xiang Y, Du Y. Research on tubular segment design of submerged floating tunnel. Procedia Eng 2010;4:199–205. https://doi.org/10.1016/j.proeng.2010.08.023.
[44] Zou PX, Bricker JD, Uijttewaal W. A parametric method for submerged floating tunnel cross-section design. Proceedings of the International Offshore and Polar Engineering Conference. 2020.
[45] Zou P, Bricker J, Uijttewaal W. Optimization of submerged floating tunnel cross section based on parametric Bézier curves and hybrid backpropagation - genetic algorithm. Mar. Struct. 2020;74:102807. https://doi.org/10.1016/j.marstruc.2020.102807.
[46] Lin H, Xiang Y, Yang Y, Chen Z. Dynamic response analysis for submerged floating tunnel due to fluid-vehicle-tunnel interaction. Ocean Eng. 2018;166:290–301. https://doi.org/10.1016/j.oceaneng.2018.08.023.
[47] Yiqiang X, Chunfeng C. Vortex-induced dynamic response analysis for the submerged floating tunnel system under the effect of currents. J. Waterway, Port, Coastal, Ocean Eng. 2013;139(3):183–9.
[48] B. Jiang, B. Liang, S. Wu, Feasibility study on the submerged floating tunnel in Qiongzhou Strait, China, Polish Marit. Res., 2018, doi: 10.2478/pomr-2018-0066.
[49] Seo S-i, Mun H-S, Lee J-h, Kim J-h. Simplified analysis for estimation of the behavior of a submerged floating tunnel in waves and experimental verification. Mar. Struct. 2015;44:142–58. https://doi.org/10.1016/j.marstruc.2015.09.002.
[50] Kunisu H. Evaluation of wave force acting on submerged floating tunnels. Procedia Eng 2010;4:99–105. https://doi.org/10.1016/j.proeng.2010.08.012.
[51] Xiao J, Huang G. Transverse earthquake response and design analysis of submerged floating tunnels with various shore connections. Procedia Eng 2010;4:233–42. https://doi.org/10.1016/j.proeng.2010.08.027.
[52] K. Kavanagh, M. Dib, E. Balch, P. Stanton, New Revision of Drilling Riser Recommended Practice (API RP 16Q), in: Proceedings of the Annual Offshore Technology Conference, 2002, doi: 10.4043/14263-ms.